buildings

MDPI

Article

Research on In Situ Stress Measurement Based on the Combined Method of DIC and Drilling Stress Relief

Lingting Ye [1], Liping Chen [1,*], Peng Zhao [2], Ruichuan Zhao [3] and Yixiang Zhou [1]

[1] Zhejiang Key Laboratory of Intelligent Construction and Operation & Maintenance for Deep-Sea Foundations, Ningbo University of Technology, Ningbo 315211, China; 15867619037@163.com (L.Y.); 15157684463@163.com (Y.Z.)
[2] Railway Engineering Research Institute, China Academy of Railway Sciences Corporation Limited, Beijing 100081, China; tieluzhaopeng@163.com
[3] China Communications Highway Planning and Design Institute Co., Ltd., Beijing 100010, China; 09125182@bjtu.edu.cn
* Correspondence: 11115302@bjtu.edu.cn

Abstract

Existing structural stress is an important parameter for evaluating the current state of a structure. In order to improve the accuracy of in situ stress measurement in the field, this paper proposes an in situ stress measurement method for existing structures, which combines Digital Image Correlation (DIC) technology with the drilling stress relief method. The method utilizes DIC technology to monitor the local displacement or strain caused by stress release from the drilled hole in real time, and further inverts the in situ stress state of the structure based on this data. First, the principle and specific implementation process of the method are introduced. Then, finite element simulations are used to analyze the influence of factors such as size effects, drill hole diameter, drill hole depth, and initial stress magnitude on the measurement results. Finally, experimental validation of the method's effectiveness is conducted. The results show that the in situ stress measurement method based on the combination of DIC and stress relief has good application effects and prospects in the stress analysis of existing structures. The accuracy and effectiveness of the method are influenced by factors such as specimen size, drill hole diameter, drill hole depth, and stress magnitude. In practical engineering, a comprehensive evaluation should be made, considering the precision of DIC testing and the magnitude of in situ stress, to select appropriate drilling parameters and measurement ranges. During the subsequent stress inversion process, a size calibration factors is applied to adjust the theoretical results, significantly improving the method's applicability under finite size conditions, and achieving good results. This research provides important references for the stress testing and evaluation of existing structures with finite sizes.

Keywords: stress measurement; digital image correlation (DIC); drilling stress relief method; size calibration factors; stress inversion

Check for updates

Academic Editor: Tomasz Sadowski

Received: 20 November 2025
Revised: 18 January 2026
Accepted: 26 January 2026
Published: 28 January 2026

Copyright: © 2026 by the authors. Licensee MDPI, Basel, Switzerland. This article is an open access article distributed under the terms and conditions of the Creative Commons Attribution (CC BY) license.

1. Introduction

Structural stress is a crucial parameter that reflects the current state of a structure and serves as an important indicator for assessing the safety performance of the structural system [1]. Currently, research in this field primarily focuses on two application scenarios: in situ stress testing and current state evaluation of existing structures, and stress state detection and safety evaluation during the construction process.

In situ structural stress state testing aims to evaluate the actual stress distribution experienced by a structure during its operational period, thereby providing scientific evidence for the assessment and maintenance of the structure's current condition. Among the methods used for in situ structural stress state detection, the drilling stress relief method is one of the most commonly applied techniques. This method was first proposed by the German scholar J. Math in 1934 [2]. The fundamental principle involves performing a pressure release operation within the structure or component, which causes a redistribution of stress, thereby generating measurable displacement or strain changes around the disturbed region. Based on these changes and using stress formulas, the stress distribution of the component can be calculated. Stress state detection during the construction process primarily aims to monitor the stress distribution throughout the construction phase, to promptly identify potential hazards and ensure the safety and stability of the construction. Common methods for stress state testing during construction include the use of embedded sensors [3,4], such as pressure boxes, rebar strain gauges, and others.

The drilling stress relief method was originally applied to the detection and evaluation of structural residual stress, aiming to prevent the accumulation of residual stress with external stress, thereby increasing the risk of structural failure. The calculation principles and formulas can be referenced from the ASTM E837-20 [5] standard and the TN-503 published by Vishay Precision Group [6]. As engineering needs have evolved, many scholars have combined the drilling stress relief method with other detection techniques, proposing new technological approaches widely applied in stress measurement of existing structures such as engineering structures and rocks. Leeman E R [7] introduced the working principle of the CSIR "Doorstopper" strain gauge, which measures strain caused by drilling and calculates stress in complex rock environments using corresponding formulas. J.W. Puller et al. [8] used the drilling method and ANZI strain units to monitor in situ stress in the overburden layer of coal mines and stress changes during hydraulic fracturing. Furthermore, they monitored changes in the pre-support load and rock layer stress during mining, providing data support for the design and safety assessment of mine support systems. Qin et al. [9] proposed a method for calculating the stress tensor in a three-layer medium using numerical simulations and established a surrogate model combining artificial neural networks (ANN). Based on this model, they developed corresponding software and validated the accuracy and effectiveness of the surrogate model in laboratory model experiments and field measurements in coal mines using the drilling method and hollow body strain gauges. Deng [10] used the drilling method to detect the residual prestress of a high-pile dock prestressed track beam, calculating the stress before drilling at the center of the beam's bottom, and then estimating the residual prestress of the in-service No. 67 prestressed track beam. Luo [11] conducted experimental tests on a prestressed concrete small box beam and calculated the existing stress of the beam using the drilling stress relief method. Pan [12] and others proposed a new method—the reinforcement drilling method—to estimate the actual stress and internal force of stressed components in existing concrete structures.

The existing stress measurement techniques are primarily based on the indirect measurement of related parameters such as strain and deformation, with stress calculated from these measurements. Therefore, accurate measurement of strain or deformation is crucial. With the development of Digital Image Correlation (DIC) technology, the use of DIC to replace traditional strain gauge methods for strain measurement has become increasingly widespread in recent years. This method was first independently proposed by I. Yamaguchi [13,14], W.H. Peters, and W.F. Ranson [15] in the early 1980s. Scholars have conducted extensive and in-depth research on the application of Digital Image Correlation (DIC) technology in structural stress measurement. Harrington et al. [16] combined the drilling method with DIC technology

to measure residual stress and structural stress separately, then subtracted the two to calculate the true structural stress. Hagara M, Trebuňa F, and Pástor M [17] used the drilling method combined with DIC technology to measure residual stress and compared the DIC results with traditional strain gauge methods and finite element simulations. The results from all three methods were in good agreement, indicating that DIC technology can effectively be used for residual stress detection. Y. Ma et al. [18] proposed a new method combining DIC technology and the drilling method to measure axially symmetric stress in cylindrical pipelines. The study showed that DIC technology could accurately measure the displacement field around the drilled hole in cylindrical pipes, which was consistent with theoretical displacement fields and numerical simulation results, as well as with stress calculations from strain gauges. Schajer G S et al. [19] introduced a full-field, multi-axis computational technique by combining the drilling method with DIC technology to determine residual stress, improving the precision of the combined method. Gao J et al. [20] proposed a new method combining DIC and the drilling method, where residual stress components were matched with deformation modes and optimized algorithms were used to maximize the similarity of image deformation data, directly matching different residual stress components to enhance measurement efficiency. M.J. McGinnis [21,22] experimentally verified the feasibility of combining DIC technology with the drilling stress relief method. Deng [23] used DIC technology combined with the stress relief method to measure in situ stress in concrete. Yang [24] validated the accuracy and reliability of the DIC-drilling stress relief method through steel beam experiments, proposing that measurements should be taken within a radius of 2 to 2.5 times the hole radius to ensure the validity of the results. Junhwa Lee [25] and Marie Allain [26] proposed combining the stress relaxation method with DIC technology to measure stress in concrete structures.

Previous studies have achieved significant progress in stress measurement using the hole-drilling stress relief method; however, several issues remain to be further investigated. Conventional deformation measurement techniques exhibit inherent limitations in acquiring deformation data after drilling. Specifically, the measurable area is highly restricted, and deformation information is typically obtained only at discrete locations where strain gauges are attached. As a result, it is difficult to capture the full-field strain or displacement distribution around the borehole. The lack of full-field data significantly limits the amount of usable information available for subsequent analysis, which may lead to considerable uncertainty or bias in the evaluation of the structural stress state. Moreover, most existing hole-drilling stress relief methods are developed based on the assumption of an infinitely large model, whereas in practical engineering applications, the tested structures usually have finite and varying dimensions. This discrepancy inevitably introduces errors associated with size effects, thereby reducing the accuracy of stress inversion results. To address these limitations, this study proposes the application of Digital Image Correlation (DIC) to stress measurement in existing structures, enabling the acquisition of full-field displacement data and effectively overcoming the problem of insufficient deformation information. In addition, based on finite element simulations, a set of size calibration coefficient formulations applicable to finite-sized specimens in engineering practice is established, thereby improving the accuracy of stress inversion for structures with finite dimensions.

2. Fundamental Principles and Process of Stress Measurement

2.1. Principle of DIC Measurement Technology

Digital Image Correlation (DIC), as an advanced optical non-contact measurement technique, offers advantages such as real-time measurement, non-contact, high precision, and full-field monitoring [27]. The technique captures images of the specimen before and after deformation using a camera, where the image taken before deformation is referred to

as the "reference image," and the image taken after deformation is called the "deformed image." By analyzing the changes in pixel intensity between corresponding positions in the two images, it enables quantitative analysis of the specimen's surface displacement and strain field.

As shown in Figure 1, the digital image correlation (DIC) measurement system consisted of a computing unit, an image acquisition device, an illumination system, and a calibration target. In this study, the quantity of interest was the surface displacement of the gypsum specimen, and the deformation was predominantly in-plane; therefore, a 2D-DIC system was employed. The hardware configuration was as follows: a Hikvision MV-CS200-10GM/GC camera (Hikvision Digital Technology Co., Ltd., Hangzhou, China) with an image resolution of approximately 20 megapixels and a maximum adjustable frame rate of 5.9 fps; a WELLS M2835-21MP-11 lens (Hunan Chiopt Optotech Co., Ltd., Changsha, China)with an f/2.8 aperture and a 35 mm focal length; a Wolfgang JZ613 tripod (Shenzhen Wolfgang Technology Co., Ltd., Shenzhen, China) as the camera mount; and a Lenovo Legion laptop (Lenovo Group Limited, Beijing, China)for data processing, which provided sufficient computational performance for subsequent analysis.

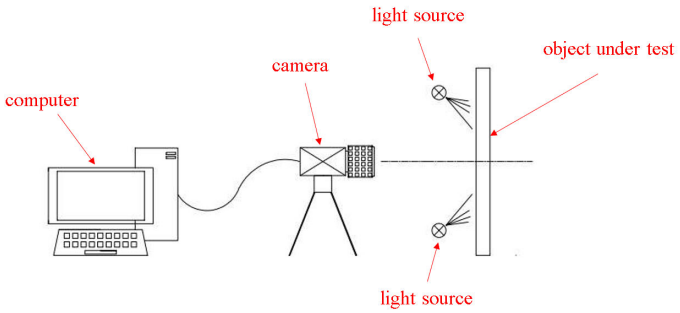


Figure 1. DIC Measurement System Schematic Diagram.

The digital image correlation (DIC) analysis in this study was performed using the commercial software GOM Correlate 2017 to process the acquired images. This software supports both two-dimensional (2D) and three-dimensional (3D) deformation analyses and is equipped with high-precision image correlation algorithms and advanced data processing capabilities, enabling accurate determination of full-field displacement and strain distributions. Additionally, it is capable of outputting the horizontal displacement (u), vertical displacement (v), Strain in the x-direction (ε_{xx}), and strain in the y-direction (ε_{yy}), as well as the maximum and minimum principal strains $(\varepsilon_{\min}, \varepsilon_{\max})$.

2.2. Distribution of Secondary Stresses and Displacements near the Borehole

Under three-dimensional stress conditions, drilling a hole inside a specimen leads to a redistribution of the local stress field, forming a secondary stress field. Assuming the specimen is an infinitely large, homogeneous, isotropic linear elastic body with a cylindrical hole perpendicular to the outer surface, a mechanical model as shown in Figure 2 is established for drilling stress analysis. It is assumed that the strain in the direction of the hole axis is constant, i.e., $\varepsilon_z = 0$. Based on the theory of elasticity, the distribution pattern of the radial absolute displacement near the hole under three-dimensional stress conditions can be derived [28,29].

$$\begin{aligned} u_{absolute} &= \frac{r}{E}\left(\frac{\sigma x+\sigma y}{2}\left[(1-\mu)+(1+\mu)\frac{a^2}{r^2}\right]+\frac{\sigma x-\sigma y}{2}(1+\mu)\left[1-\frac{a^4}{r^4}+4(1-\mu)\frac{a^2}{r^2}\right]cos2\theta+\right. \\ &\left.\tau_{xy}(1+\mu)\left[1-\frac{a^4}{r^4}+4(1-\mu)\frac{a^2}{r^2}\right]sin2\theta-\mu\sigma z\right) \end{aligned} \quad (1)$$

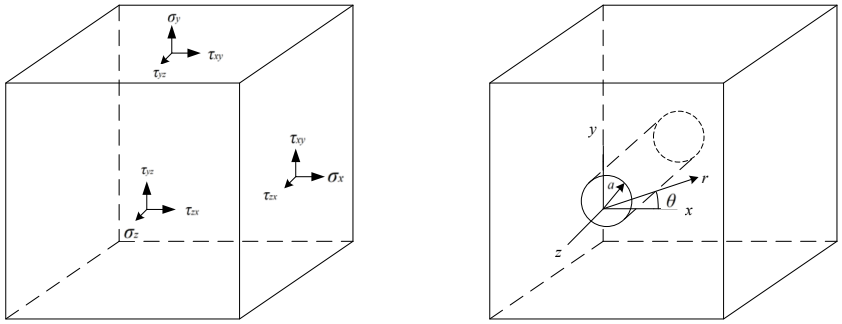


Figure 2. Secondary stress field of drilling.

Radial displacement is defined as the radial absolute displacement after drilling minus the original radial displacement before drilling. The expression for the original radial displacement $u0$ before drilling is as follows:

$$u0 = \frac{r}{E}\left(\frac{\sigma x+\sigma y}{2}[(1-\mu)] + \frac{\sigma x-\sigma y}{2}(1+\mu)\,cos2\theta + \tau_{xy}(1+\mu)sin2\theta - \mu\sigma z\right) \quad (2)$$

Therefore, the radial displacement u is given by:

$$\begin{aligned} u = \; & \frac{r}{E}\left(\frac{\sigma x+\sigma y}{2}\left[(1+\mu)\frac{a^2}{r^2}\right] + \frac{\sigma x-\sigma y}{2}(1+\mu)\left[-\frac{a^4}{r^4}+4(1-\mu)\frac{a^2}{r^2}\right]cos2\theta + \right. \\ & \left.\tau_{xy}(1+\mu)\left[-\frac{a^4}{r^4}+4(1-\mu)\frac{a^2}{r^2}\right]sin2\theta\right) \end{aligned} \quad (3)$$

In the equation, r is the radial distance, in meters (m); E is the Young's modulus, in Pascals (Pa); μ is the Poisson's ratio; a is the radius of the hole, in meters (m); and θ is the angle between the radial distance and the 0° direction, °.

In the local deformation caused by drilling, displacement variations in the 0° and 90° directions primarily occur along the radial direction. Although there are some displacement variations in the circumferential and axial directions, these changes are relatively small. Therefore, this study focuses on radial displacement as the main subject of research.

2.3. Principle and Process of Stress Inversion

Based on the radial displacement formulation, the in situ stress is determined through inversion using the Particle Swarm Optimization (PSO) algorithm [30]. In this algorithm, σ_x and σ_y are treated as independent variables, and the corresponding u values of σ_x and σ_y are treated as dependent variables. According to Equation (4), by minimizing $J(\sigma_x,\ \sigma_y)$, the optimal solution is obtained, thereby achieving the precise inversion of the stress results.

$$J(\ \sigma_x,\ \sigma_y) = \|u_{inverted} - u_{Measured}\|_2^2 \quad (4)$$

In the equation, $J(\sigma_x, \sigma_y)$ represents the sum of the squared differences between the theoretical value and the measured value. The specific process is shown in Figure 3.

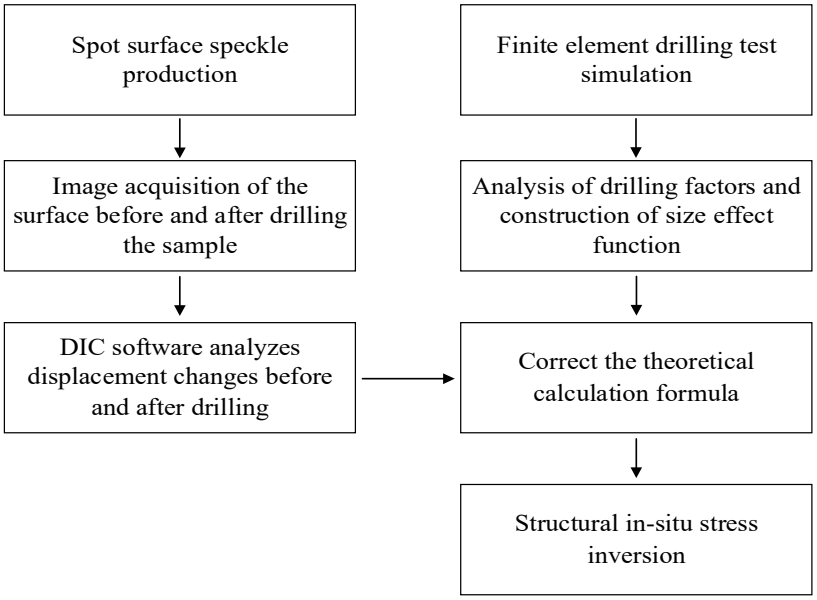


Figure 3. Total process analysis diagram.

3. Numerical Simulations and Results

3.1. Computational Model and Parameters

In this study, numerical simulations were conducted using the Standard module in ABAQUS (2021) to investigate the radial displacement variations induced by drilling. A three-dimensional finite element model with geometric dimensions of 150 mm × 150 mm × 150 mm was established using solid elements to examine the effects of drilling depth, hole diameter, and initial stress magnitude on the radial displacement around the borehole. Subsequently, models with sizes ranging from 150 mm to 4650 mm were developed to explore the influence of size effects on radial displacement. The numerical model was formulated based on the following assumptions: with respect to the constitutive behavior, a linear elastic constitutive model was adopted, and the material parameters included density, elastic modulus, and Poisson's ratio, with specific values listed in Table 1; regarding boundary conditions, rotational degrees of freedom were constrained on the upper surface as well as the front, back, left, and right surfaces, while the bottom surface was fully fixed, and an initial stress was applied to the upper surface to ensure that the model remained in a pre-existing stress state; in terms of mesh discretization, the C3D8R element type was employed, and the model was meshed using a combination of structured and swept meshing techniques, with a global mesh size of 5 mm × 5 mm, while a locally refined mesh was generated in the drilling region using the neutral axis algorithm within the swept meshing approach; when simulating the drilling process in a pre-stressed structure, a static general analysis procedure was adopted, as the present study primarily focuses on the effect of drilling on the radial displacement at the structural surface, and the drilling process was modeled using the element activation and deactivation technique, with dynamic effects during drilling neglected. Figure 4 illustrates the schematic of the finite element model.

Table 1. Mechanical parameters of gypsum specimens.

Parameter	Value	Unit
Density	1.84	$\rho/g{\cdot}cm^{-3}$
Elastic Modulus	1363	E/MPa
Poisson's Ratio	0.2	/
Uniaxial Compressive Strength	22.37	MPa

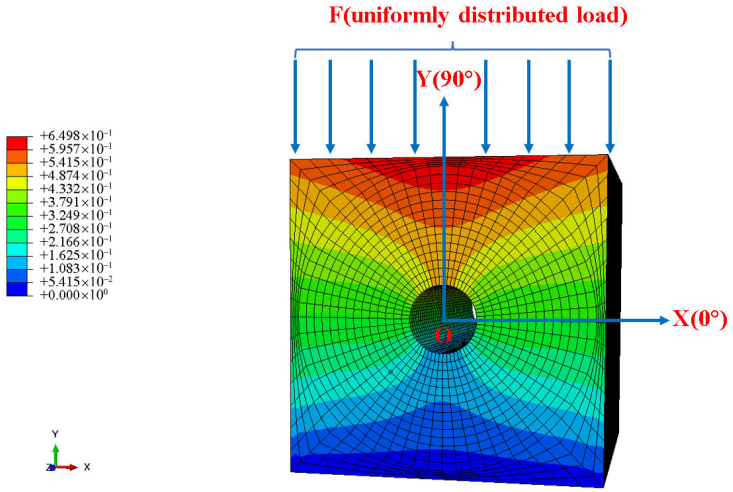
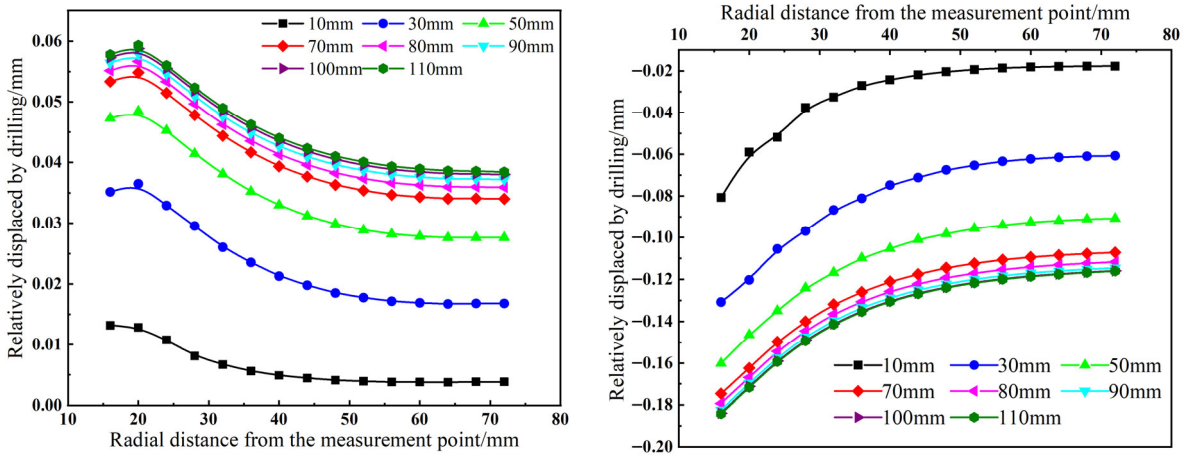


Figure 4. Schematic diagram of the model after drilling.

When analyzing the drilling-induced changes in surface radial displacement, the 0° and 90° directions are selected as the observation directions because they can effectively capture the displacement trends caused by drilling and provide highly comparable displacement data. Specifically, the 0° direction refers to the direction along the *x*-axis, which is perpendicular to the loading direction; the 90° direction refers to the direction along the *y*-axis, which is parallel to the loading direction.

3.2. The Effect of Borehole Depth on Surface Radial Displacement

To analyze the effect of different drilling depths on surface displacement variation, a simulation was conducted with an initial stress of 5 MPa and a hole diameter of 32 mm as the initial conditions. The impact of different drilling depths on radial displacement was investigated. The drilling depth ranged from 10 mm to 110 mm, and the variation in displacement with depth is shown in Figure 5.



(**a**) Radial displacement in the 0° direction

(**b**) Radial displacement in the 90° direction

Figure 5. Radial displacement at different drilling depths.

As shown in Figure 5a, with the increase in radial distance, the radial displacement in the 0° direction initially shows a slight increase, then gradually decreases and tends to stabilize. Figure 5b indicates that in the 90° direction, the radial displacement decreases monotonically with the increase in radial distance. When the radial distance reaches 60 mm (1.87 times the hole diameter), the surface displacement variation becomes stable.

Figure 6 illustrates the effect of drilling depth on displacement variation. As seen in the figure, the radial displacement does not increase linearly or infinitely with the increase in drilling depth. Initially, the radial displacement varies significantly with drilling depth, but as the drilling depth increases, the displacement variation gradually stabilizes. In particular, when the drilling depth reaches 100 mm (3 times the hole diameter), the displacement variation stabilizes.

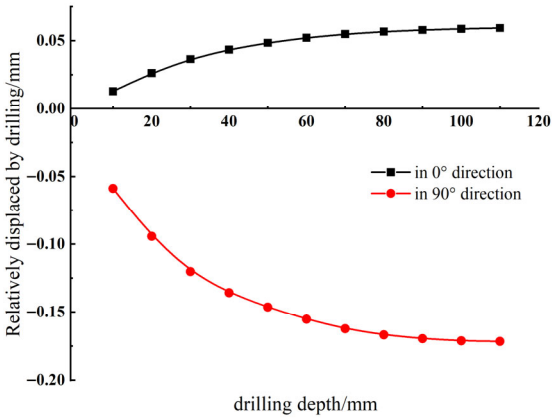


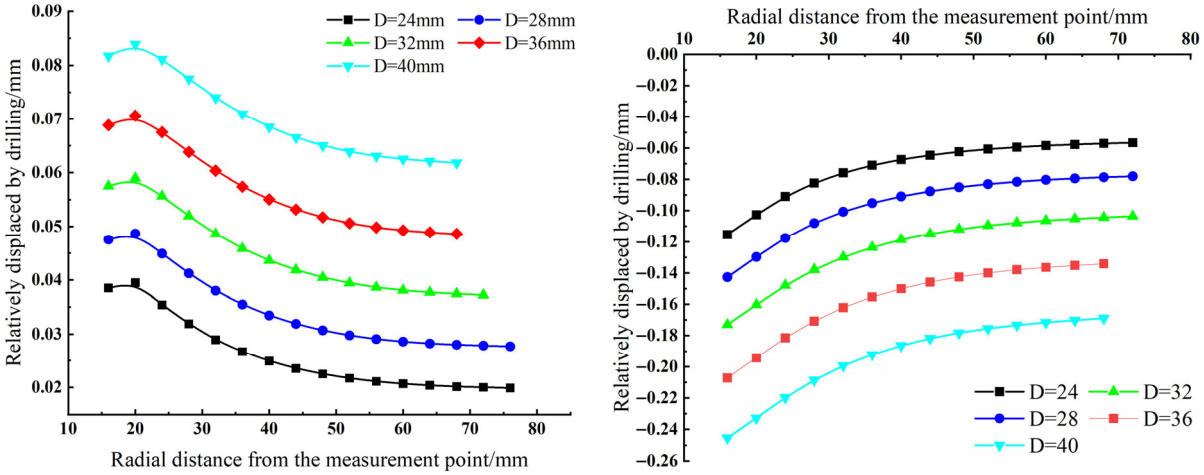
Figure 6. Radial displacement variation diagram at 20mm radial distance.

In summary, under an initial stress of 5 MPa and a borehole diameter of 32 mm, the drilling-induced radial displacement increases progressively with increasing drilling depth, indicating an increasingly pronounced deformation response associated with local stress relief. When the drilling depth reaches 100 mm, corresponding to three times the borehole diameter, the radial displacement tends to stabilize. Therefore, under these conditions, the additional influence of further increasing the drilling depth on surface displacement can be considered negligible. Meanwhile, the displacement effect induced by drilling on the surrounding region diminishes with increasing radial distance; when the radial distance reaches 60 mm, approximately 1.87 times the borehole diameter, its influence can likewise be neglected within the scope of the present study.

3.3. The Effect of Borehole Diameter on Surface Radial Displacement

To investigate the effect of different hole diameters on surface displacement variation, a simulation was conducted with an initial stress of 5 MPa and a drilling depth of 150 mm as the initial conditions. The changes in surface radial displacement were studied for five different hole diameters: 24 mm, 28 mm, 32 mm, 36 mm, and 40 mm.

As shown in Figure 7, with the increase in hole diameter, the radial displacement in both the 0° and 90° directions increases significantly, indicating that the increase in hole diameter strengthens the displacement response in the region around the hole. Figure 8 shows the variation trend of the peak radial displacement for different hole diameters. The results indicate that as the hole diameter increases, the absolute value of the displacement peak caused by the hole exhibits an approximately linear growth trend. By comparing the peak values in the two directions, it can be observed that, under the same hole diameter conditions, the absolute value of the displacement peak in the 90° direction is significantly higher than that in the 0° direction (approximately three times greater). This phenomenon suggests that, under unidirectional compression, the stress release caused by the hole has a more significant effect on the surface displacement in the loading direction (90° direction).



(**a**) Radial displacement in the 0° direction (**b**) Radial displacement in the 90° direction

Figure 7. Radial displacement under different borehole diameters.

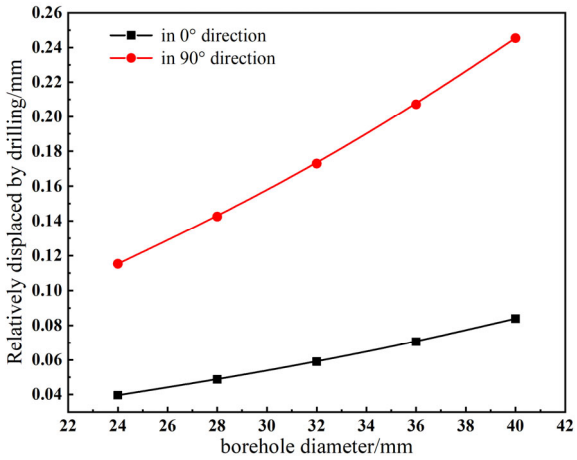


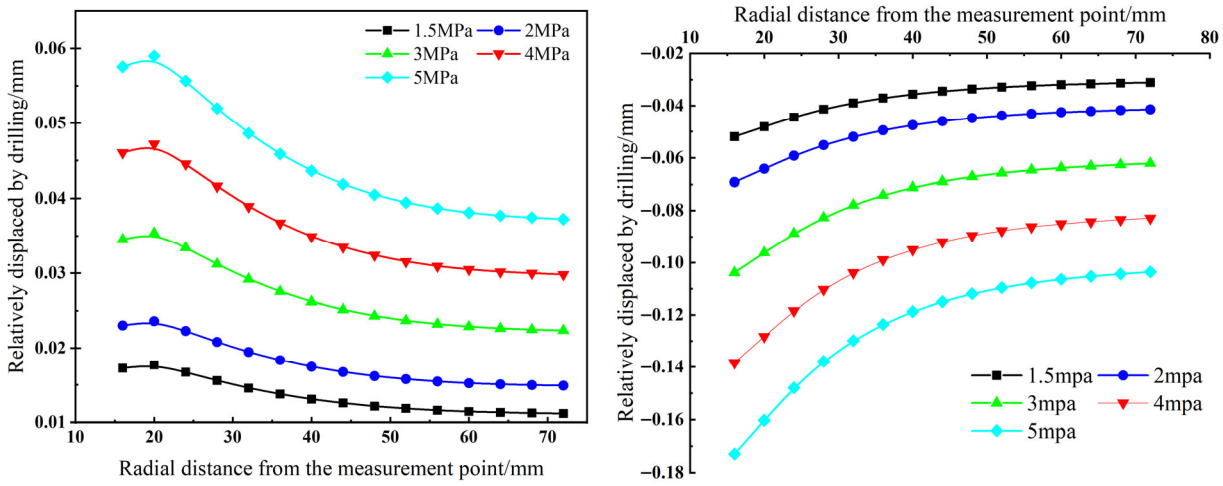
Figure 8. Comparison of radial displacement peak under different borehole diameters.

3.4. The Effect of Initial Stress Magnitude on Surface Radial Displacement

To study the effect of initial stress magnitude on surface displacement variation, a numerical simulation was conducted with a hole diameter of 32 mm and a drilling depth of 150 mm as the initial conditions. The initial stresses were set to 1.5 MPa, 2 MPa, 3 MPa, 4 MPa, and 5 MPa, corresponding to five different conditions. The variation in radial displacement near the drilling area under different initial stress conditions was investigated.

The data in Figure 9 show that with the increase in initial stress, the radial displacement in both the 0° and 90° directions exhibits a monotonically increasing trend. Especially when the initial stress is low, the displacement variation around the hole is relatively gradual. As the stress increases, the amplitude of the displacement variation also increases, reflecting the significant impact of initial stress changes on the displacement around the hole.

Based on the accuracy of the Digital Image Correlation (DIC) equipment used in this experiment, which is 0.01 mm, it can be seen from the data in Figure 9a that when the initial stress is 1.5 MPa, the radial displacement in the 0° direction approaches the measurement limit of the DIC equipment. Therefore, 1.5 MPa can be considered as the critical stress value for this DIC system. When the stress is below this value, the equipment cannot provide sufficient measurement accuracy, leading to the inability to obtain valid displacement data.

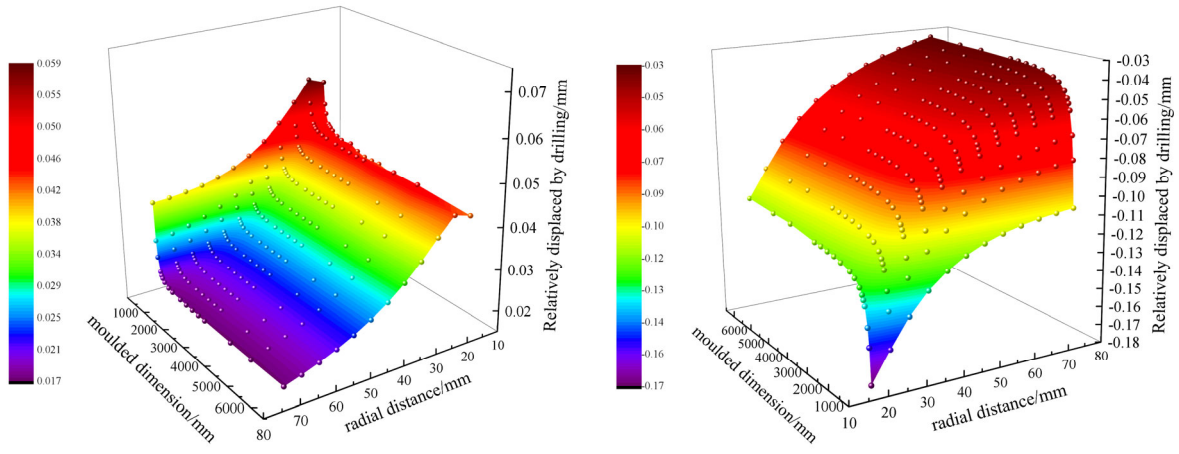


(**a**) Radial displacement in the 0° direction (**b**) Radial displacement in the 90° direction

Figure 9. Radial displacement under different initial stresses.

3.5. The Effect of Model Size on Surface Radial Displacement

To reduce the bias induced by size effects, a size calibration coefficient is introduced to correct the theoretical predictions derived under the infinite-domain assumption (i.e., Equation (3)). Figure 10 presents the numerically simulated radial displacements along the 0° and 90° directions obtained for a borehole diameter of 32 mm and an in situ stress of 5 MPa, where all other parameters are kept unchanged and only the model geometry is varied by progressively increasing the specimen size from 150 mm × 150 mm × 150 mm to 4650 mm × 4650 mm × 4650 mm. By comparing the numerical results with the theoretical solutions based on the infinite-domain model, it is observed that when the model size reaches 4650 mm, corresponding to approximately 145 times the borehole diameter, the theoretical predictions and numerical simulations exhibit nearly perfect agreement.



(**a**) Radial displacement in the 0° direction (**b**) Radial displacement in the 90° direction

Figure 10. Radial displacement at different model sizes.

Based on the above simulation results, radial distance and model size were introduced as governing parameters to allow the simulated results at different model sizes and radial

positions to approach the corresponding theoretical solutions, thereby establishing a size calibration coefficient. The explicit form of the size calibration coefficient is given as follows:

$$u_{theory} = f(x, L)u_{sim} \tag{5}$$

$$f^{0^\circ}(x,L) = \frac{u^{0^\circ}_{theory}}{u^{0^\circ}_{sim}} = \frac{4.6 + 0.18x - 0.15L}{0.15x - 0.15L} \tag{6}$$

$$f^{90^\circ}(x,L) = \frac{u^{90^\circ}_{theory}}{u^{90^\circ}_{sim}} = \frac{-0.5 - 0.1x + 0.1L}{2.5 + 0.1x + 0.1L} \tag{7}$$

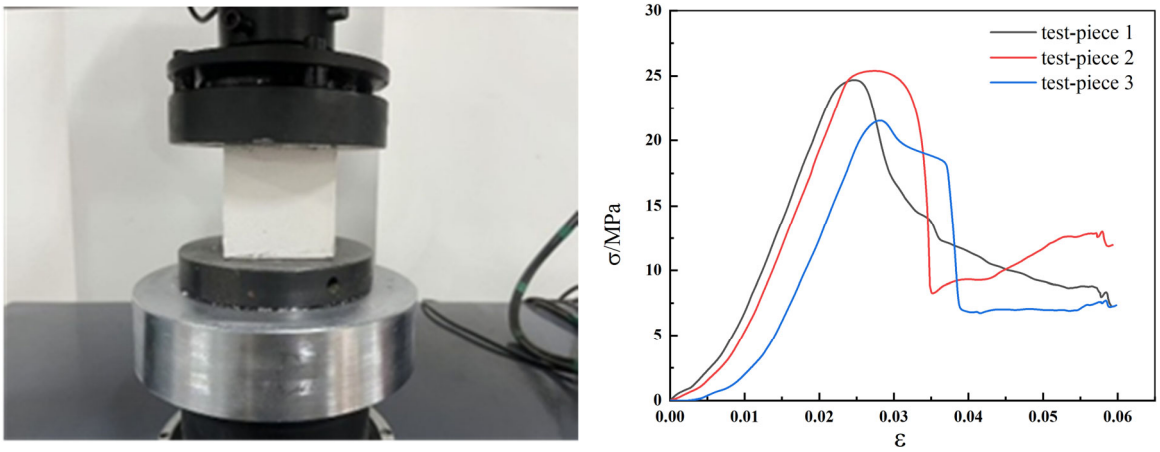
In the equation: u_{sim} is the radial displacement obtained from numerical simulation; u_{theory} is the radial displacement obtained from theoretical calculation; L represents the model size; x is the radial distance, representing the radial distance from the measurement point to the center of the hole; and $f(x,L)$ is the size calibration factors. It should be noted that this size calibration coefficient is applicable only to the case with a 32 mm drilling diameter; for other hole diameters, the corresponding coefficient can be derived following the same procedure.

4. Specimen Preparation and Data Acquisition

4.1. Preparation of Specimens and Mechanical Properties

The gypsum specimens are made using high-strength gypsum powder as the raw material, mixed in a mass ratio of water to gypsum powder of 1:3.28. After curing and molding, the specimens are demolded and cured under normal temperature conditions.

Mechanical performance tests were conducted using a testing machine, as shown in Figure 11a. The mechanical performance test results of the gypsum specimens are shown in Figure 11b, and the measured physical and mechanical parameters, such as Young's modulus and uniaxial compressive strength, are listed in Table 1.



(**a**) Mechanical properties test (**b**) Test specimen stress–strain curve

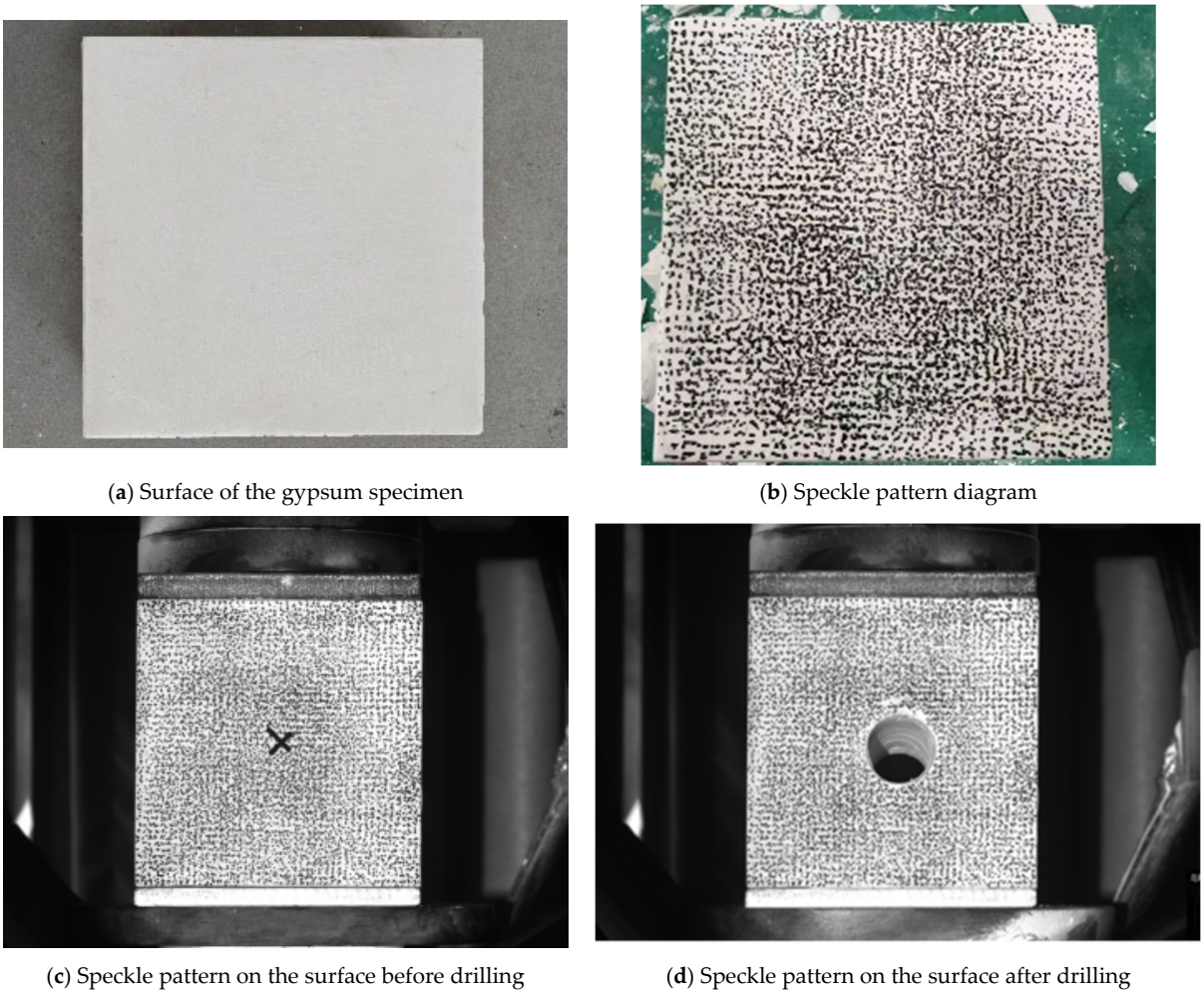
Figure 11. Test of gypsum specimen parameters and test results.

4.2. Experimental Design

To simulate the practical conditions of in situ stress measurement in existing structures using the borehole stress-relief method, a "load-first, drill-later" experimental protocol was employed. The displacement field induced during drilling was measured using digital image correlation (DIC), and the initial stress state was subsequently inverted based on

the corresponding stress calculation formulations. It should be emphasized that the initial stress obtained in this study represents the superposition of the externally applied load and the residual stress generated during specimen fabrication. The detailed experimental procedures are described below.

The first step is to polish the measurement surface of the gypsum specimen with sandpaper to ensure a flat and smooth surface (Figure 12a). The second step is to create a speckle pattern using black and white spray paint; the speckles should be distributed as uniformly as possible to avoid overly dense or sparse regions (Figure 12b). The third step involves the installation and calibration of the DIC measurement system. Since a single-camera configuration is adopted in the experiment, the camera is aligned to be parallel to the specimen surface during installation by adjusting the height of the camera mount and using the built-in spirit level to center the bubble, thereby ensuring proper alignment between the camera and the specimen surface. The fourth step is to apply the load incrementally at a rate of 1 kN/s. The load is held for 30 s at 40 kN to ensure sufficient preloading; thereafter, a 30 s dwell time is maintained at each subsequent 20 kN increment until the load reaches 112.5 kN (5 MPa), after which the pressure is kept constant. The fifth step is to capture an image of the un-drilled specimen as the reference image for subsequent analysis (Figure 12c). The sixth step is to drill the specimen using a 32 mm diameter drill with a through-hole configuration; after drilling, a post-relief speckle image is acquired (Figure 12d).



(**a**) Surface of the gypsum specimen

(**b**) Speckle pattern diagram

(**c**) Speckle pattern on the surface before drilling

(**d**) Speckle pattern on the surface after drilling

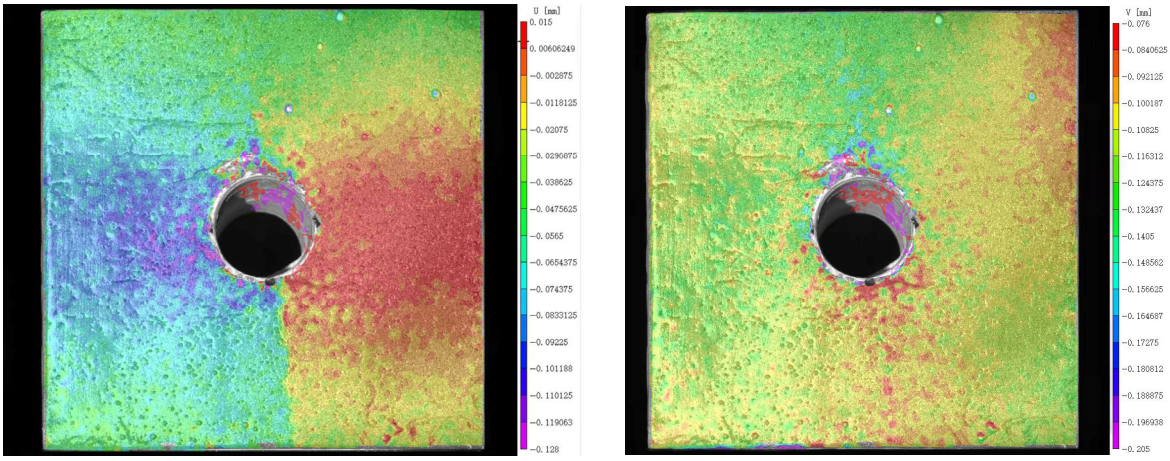
Figure 12. Data collection and overall experiment process.

5. Experimental Data Analysis

5.1. Selection of Displacement Measurement Points

Before image analysis, the captured images were renamed and imported into GOM Correlate 2017 in a sequential order (i.e., "1", "2", "3", . . .) in accordance with the software requirements. First, the specimen scale was calibrated by selecting two corner points with a known distance in the image and inputting the corresponding physical distance, allowing the software to establish the spatial scale. After calibration, the scale parameters were automatically updated for all images. Next, a region of interest (ROI)—i.e., the analysis surface—was defined for the measurement area. For the analysis settings, the default subset and step sizes in GOM Correlate 2017 were adopted, with a subset size of 19 × 19 pixels and a step size of 16 pixels.

Figure 13 shows the radial displacement results in the 0° and 90° directions obtained through DIC software (GOM Correlate 2017) analysis after drilling the specimen. During the drilling process, friction between the drill and the gypsum caused slight damage around the hole, disrupting the integrity of the speckle pattern and preventing it from being recognized, which in turn affected the software's analysis results. To avoid such interference, measurement points should be chosen at a certain distance from the hole edge to avoid being too close to the hole wall. At the same time, considering that stress concentration and deformation mainly occur in the region near the hole during drilling, measurement points should not be set too far away. Based on finite element analysis results and the measurement accuracy of the DIC equipment, the measurement area was selected within a range of 1 to 2 times the hole diameter. This approach avoids interference from surface damage around the hole while ensuring that the collected data accurately reflects the variation in radial displacement during the drilling stress relief process. The measurement points are arranged starting from a radial distance of 36 mm, with intervals of 5 mm, up to a distance of 56 mm, with five measurement points set in each direction. This arrangement allows the capture of displacement changes at different locations and provides more precise displacement data for subsequent analysis of the surface displacement of the gypsum specimen under constant pressure.



(**a**) 0° direction analysis results (**b**) 90° direction analysis results

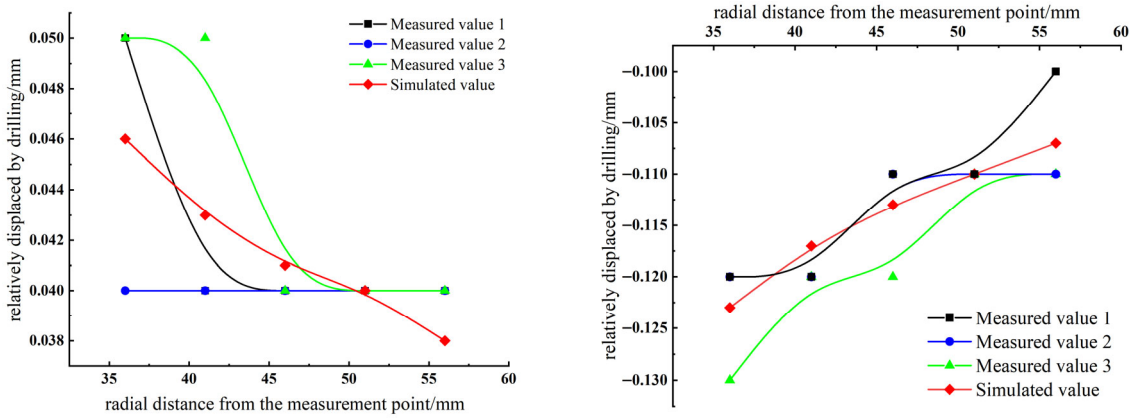
Figure 13. DIC analysis results after drilling.

5.2. Validation of the Numerical Model

Figure 14 compares the three sets of experimental measurements with the numerical simulation results in the 0° and 90° directions. To more comprehensively evaluate the

agreement between the numerical model and the experimental results, the root mean square error (*RMSE*) is adopted as the error metric, and its definition is given in Equation (8). Table 2 reports, for both the 0° and 90° directions, the maximum absolute differences and the corresponding *RMSE* values between the measured displacements and the simulated results for the three test sets. In the 0° direction, the maximum absolute difference is 0.007 mm, and the maximum *RMSE* is 0.004 mm; in the 90° direction, the maximum absolute difference is 0.007 mm, and the maximum *RMSE* is 0.005 mm. These comparisons indicate that the discrepancy between the numerical predictions and the measurements is minimal, demonstrating the high accuracy and validity of the proposed numerical model.

$$RMSE = \sqrt{\frac{1}{n}\sum_{i=1}^{n}(u_{measured} - u_{simulated})^2} \tag{8}$$



(**a**) Comparison results in the 0° direction (**b**) Comparison results in the 90° direction

Figure 14. Comparison between measured values and simulated values.

Table 2. Comparison and Analysis of Measured Data and Numerical Simulation Results.

Analysis Direction	Test Set	Deviation	*RMSE*
0°	Set 1	0.004	0.002
	Set 2	0.006	0.003
	Set 3	0.007	0.004
90°	Set 1	0.007	0.004
	Set 2	0.003	0.003
	Set 3	0.007	0.005

5.3. Comparative Analysis of Measured Values, Theoretical Values, and Corrected Theoretical Values

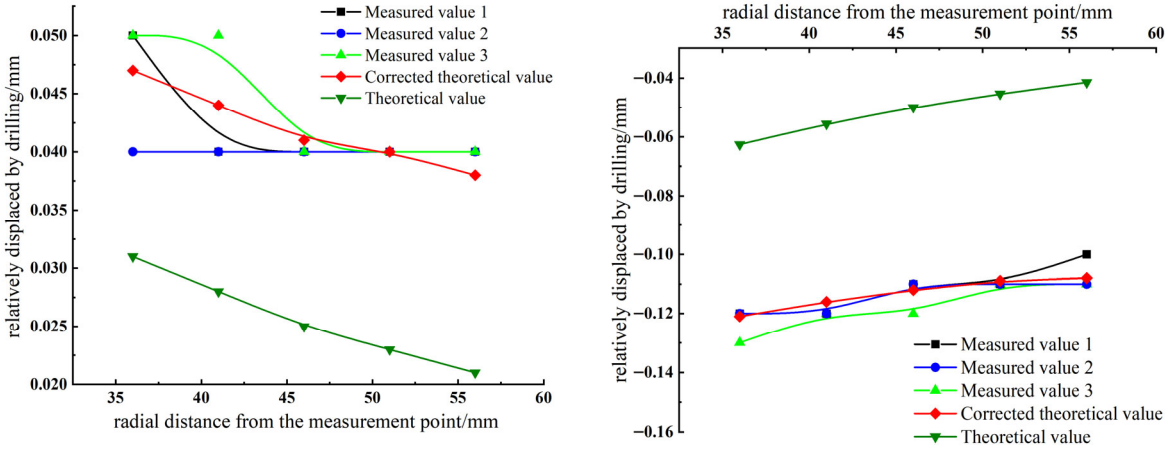
In this experiment, specimens with dimensions of 150 mm × 150 mm × 150 mm were employed. By incorporating the above-mentioned size calibration coefficient, the existing theoretical formulation was modified, and the resulting corrected theoretical expression is given as follows:

$$u^{0^\circ}_{Corrected\ theoretical\ value} = \frac{(0.15x-22.5)r}{(0.18x-17.9)E}\left(\frac{\sigma x+\sigma y}{2}\left[(1+\mu)\frac{a^2}{r^2}\right] + \frac{\sigma x-\sigma y}{2}(1+\mu)\left[-\frac{a^4}{r^4}+4(1-\mu)\frac{a^2}{r^2}\right]cos2\theta + \tau_{xy}(1+\mu)\left[-\frac{a^4}{r^4}+4(1-\mu)\frac{a^2}{r^2}\right]sin2\theta\right) \tag{9}$$

$$u^{90^\circ}_{Corrected\ theoretical\ value} = \frac{(17.5+0.1x)r}{(14.5-0.1x)E}\left(\frac{\sigma x+\sigma y}{2}\left[(1+\mu)\frac{a^2}{r^2}\right] + \frac{\sigma x-\sigma y}{2}(1+\mu)\left[-\frac{a^4}{r^4}+4(1-\mu)\frac{a^2}{r^2}\right]cos2\theta + \tau_{xy}(1+\mu)\left[-\frac{a^4}{r^4}+4(1-\mu)\frac{a^2}{r^2}\right]sin2\theta\right) \tag{10}$$

Figure 15 compares the theoretical values, the corrected theoretical values, and the experimental measurements along the 0° and 90° directions. To evaluate the effectiveness of the size calibration coefficient, the mean absolute error (*MAE*) is adopted as the error metric, and its calculation is given in Equation (11). Tables 3 and 4 summarize, for the 0° and 90° directions, respectively, the maximum absolute differences between the experimental measurements and the theoretical values, as well as between the experimental measurements and the corrected theoretical values; the corresponding *MAE* values for the three test sets are also reported.

$$MEA = \frac{1}{n}\sum_{i=1}^{n}\left|u_{measured} - u_{Theoretical/Corrected\ theoretical}\right| \tag{11}$$



(**a**) Comparison results in the 0° direction

(**b**) Comparison results in the 90° direction

Figure 15. Comparison of theoretical value, revised theoretical value and measured value.

Table 3. Maximum Deviation Table.

Analysis Direction	Test Set	Theoretical vs. Measured	Corrected Theoretical vs. Measured
0°	Set 1	0.019	0.004
	Set2	0.019	0.007
	Set 3	0.022	0.006
90°	Set 1	0.065	0.008
	Set2	0.069	0.004
	Set 3	0.07	0.009

Table 4. Mean Absolute Error Table.

Analysis Direction	Test Set	Theoretical vs. Measured	Corrected Theoretical vs. Measured
0°	Set 1	0.016	0.002
	Set2	0.014	0.003
	Set 3	0.018	0.002
90°	Set 1	0.061	0.003
	Set 2	0.063	0.002
	Set 3	0.067	0.005

As summarized in Table 3, without considering the size calibration coefficient, the maximum absolute difference between the experimental measurements and the theoretical

values is 0.022 mm in the 0° direction and 0.070 mm in the 90° direction (across the three test sets). After introducing the size calibration coefficient, the maximum absolute difference decreases to 0.007 mm in the 0° direction and 0.009 mm in the 90° direction. Table 4 further shows that, before applying the size calibration coefficient, the MAE is 0.018 mm in the 0° direction and 0.067 mm in the 90° direction; after calibration, the MAE is reduced to 0.003 mm and 0.005 mm, respectively. These results indicate that the size calibration coefficient substantially reduces the discrepancy between the theoretical predictions and the experimental measurements, confirming that it improves the accuracy of radial-displacement predictions for finite-sized models.

5.4. Stress Inversion Based on DIC Results

To investigate the feasibility of combining the DIC technique with the stress relief method for in situ stress measurement in existing structures, the DIC-measured results from three test groups were substituted into the modified theoretical Equations (9) and (10). In conjunction with the particle swarm optimization algorithm, the initial stress applied to the specimens was inversely identified, and the corresponding calculated results are summarized in Table 5.

Table 5. In-plane stress comparison table.

	Stress Parameter	Actual Stress (MPa)	Inversion Result (MPa)
Specimen 1	σ_y	−5	−4.97
	σ_x	0	0.02
Specimen 2	σ_y	−5	−5.16
	σ_x	0	−0.24
Specimen 3	σ_y	−5	−5.24
	σ_x	0	0.02

As shown in Table 5, the applied initial stress is −5 MPa. The initial stresses inverted for the three specimens are −4.97 MPa, −5.16 MPa, and −5.24 MPa, respectively. The maximum absolute error is 0.24 MPa, corresponding to a maximum relative error of 4.8%, which is below the 5% tolerance and thus meets typical engineering requirements. These results validate that the proposed approach combining DIC with the drilling stress-relief method can accurately evaluate the in situ stress in the structure.

5.5. Discussion on the DIC-Hole-Drilling Stress Relief Method

Based on the aforementioned study, it can be concluded that the DIC-hole-drilling stress relief method is effective for measuring in situ stresses within structures. However, several key issues must be considered in its practical application. First, drilling is an essential operation during the testing process; however, this procedure inevitably interferes with the structural integrity, potentially leading to localized damage or reduced local stability. Second, the measurement results and subsequent stress inversion process are significantly constrained by the precision of the Digital Image Correlation (DIC) technique. When the strain level falls below the effective resolution of the DIC system, reliable displacement or strain fields cannot be obtained, thereby compromising the accuracy of the inferred stress state. Therefore, in field measurements, it is recommended to select measurement points in areas with relatively high in situ stress levels, as higher stresses generate more significant strain signals, which can improve measurement accuracy. Additionally, a smaller hole diameter and an appropriate drilling depth should be employed during drilling to minimize the adverse effects of drilling on the structural performance.

6. Conclusions

This paper explores a method for measuring in situ stress in existing structures by combining Digital Image Correlation (DIC) technology with the drilling stress relief method. The method uses DIC technology to capture full-field deformation data around the hole, and based on this data, the in situ stress state of the structure is further inverted. Finite element simulations were used to analyze the impact of factors such as Model size, hole diameter, drilling depth, and initial stress magnitude on the test results, providing a theoretical basis for selecting hole parameters and testing ranges in the experiment. Based on the above research results, the following main conclusions are drawn:

(1) The combination of DIC technology and the stress relief method shows good application performance in in situ stress testing of existing structures. At the same time, DIC technology can collect full-field deformation data from the surface, solving the problem where traditional deformation measurement methods can only obtain point deformation data from local areas.

(2) By establishing a size calibration coefficient, the theoretical calculation results were corrected, thereby improving the accuracy of stress inversion for structural components of different sizes and enhancing the practical applicability of the theoretical formulation in engineering applications.

(3) During the testing process, the drilling depth should be selected as three times the hole diameter, and the measurement area should be chosen within a range of 1 to 2 times the hole diameter. Data within this range not only reflects the variation in radial displacement during the drilling stress relief process but also avoids software recognition failure caused by speckle pattern damage, thereby improving the accuracy and reliability of the measurement data.

Author Contributions: Conceptualization, L.C. and R.Z.; methodology, L.C.; software, L.Y.; validation, L.C., and L.Y.; formal analysis, L.C. and L.Y.; investigation, R.Z. and P.Z.; resources, R.Z. and P.Z.; data curation, Y.Z.; writing—original draft preparation, L.Y.; writing—review and editing, L.C.; visualization, L.C.; supervision, L.C.; project administration, L.C., and R.Z.; funding acquisition, P.Z. and R.Z. All authors have read and agreed to the published version of the manuscript.

Funding: This work was supported by the National Natural Science Foundation of China under Grant No. U2469207.

Data Availability Statement: The data presented in this study are available from the first author upon reasonable request.

Acknowledgments: Thanks are due to Jia-Kang Chen and Bo-Xian Tang for their assistance during the experimental process.

Conflicts of Interest: The authors Zhao Ruichuan and Zhao Peng are, respectively, from Railway Engineering Research Institute, China Academy of Railway Sciences Corporation Limited. and China Communications Highway Planning and Design Institute Co., Ltd. The remaining authors declare that the research was conducted in the absence of any commercial or financial relationships that could be construed as a potential conflict of interest.

Abbreviations

The following abbreviations are used in this manuscript:

DIC	Digital Image Correlation
PSO	Particle Swarm optimization

References

1. Zhao, Y. Experimental Study of the Working Stress State of Concrete Frame Structures through Ultrasonic Testing. Master's Thesis, Hebei Agricultural University, Baoding, China, 2018.
2. Mathar, J. Determination of initial stresses by measuring the deformations around drilled holes. *Trans. Am. Soc. Mech. Eng.* **1934**, *56*, 249–254. [CrossRef]
3. Zhou, X.Q. Research on Construction Mechanic and Stability Control Technology of Four Hole Small Spacing Tunnel. Master's Thesis, Qingdao University of Technology, Qingdao, China, 2024.
4. Sun, Z.C.; Lu, Q.Q.; Sun, F.X. Surrounding Rock Load and Segment Mechanical Behavior of Chunfeng Road Super-Large Diameter Shield Tunnel. *Tunn. Constr.* **2024**, *44*, 85–92.
5. *ASTM E837-20*; Standard Test Method for Determining Residual Stresses by the Hole-Drilling Strain-Gage Method. ASTM International: West Conshohocken, PA, USA, 2020.
6. VISHAY Measurements Group. *Measurement of Residual Stresses by the Hole-Drilling Strain Gage Method*; Tech note TN-503-6; VISHAY Measurements Group: Wendell, NC, USA, 2010; p. 11053.
7. Leeman, E.R. The CSIR "Doorstopper" and triaxial rock stress measuring instruments. *Rock Mech. Rock Eng.* **1971**, *3*, 25–50. [CrossRef]
8. Puller, J.W.; Mills, K.W.; Jeffrey, R.G.; Walker, R.J. In-situ stress measurements and stress change monitoring to monitor overburden caving behaviour and hydraulic fracture pre-conditioning. *Int. J. Min. Sci. Technol.* **2016**, *26*, 103–110. [CrossRef]
9. Qin, C.; Zhao, W.; Chen, W.; Xie, P.; Zhou, S. A surrogate model for estimating rock stress by a hollow inclusion strain cell in a three-layer medium. *Int. J. Min. Sci. Technol.* **2025**, *35*, 363–381. [CrossRef]
10. Deng, L.F. Residual Prestress Detection Technique Research and Application for Prestressed Members of High-Piled Wharf. Master's Thesis, Changsha University of Science & Technology, Changsha, China, 2011.
11. Luo, J.B. Further Study About Existing Stress Testing of the Prestress Small Box Girder by Using Stress Relief Method Based Drilling. Master's Thesis, South China University of Technology, Guangzhou, China, 2013.
12. Pan, L.; Li, Z.W. Research on the new polytechnic method of determination for actual stresses in reinforced concrete members. *Build. Struct.* **2013**, *43*, 73–80.
13. Yamaguchi, I. Speckle displacement and decorrelation in the diffraction and image fields for small object deformation. *Opt. Acta Int. J. Opt.* **1981**, *28*, 1359–1376. [CrossRef]
14. Yamaguchi, I. A laser-speckle strain gauge. *J. Phys. E Sci. Instrum.* **1981**, *14*, 1270. [CrossRef]
15. Peters, W.H.; Ranson, W.F. Digital imaging techniques in experimental stress analysis. *Opt. Eng.* **1982**, *21*, 427–431. [CrossRef]
16. Harrington, J.S.; Schajer, G.S. Measurement of structural stresses by hole-drilling and DIC. *Exp. Mech.* **2017**, *57*, 559–567. [CrossRef]
17. Hagara, M.; Trebuňa, F.; Pástor, M.; Huňady, R.; Lengvarský, P. Analysis of the aspects of residual stresses quantification performed by 3D DIC combined with standardized hole-drilling method. *Measurement* **2019**, *137*, 238–256. [CrossRef]
18. Ma, Y.; Yao, X.; Zhang, D. Axially symmetrical stresses measurement in the cylindrical tube using DIC with hole-drilling. *Opt. Lasers Eng.* **2015**, *66*, 174–180. [CrossRef]
19. Schajer, G.S.; Winiarski, B.; Withers, P.J. Hole-drilling residual stress measurement with artifact correction using full-field DIC. *Exp. Mech.* **2013**, *53*, 255–265. [CrossRef]
20. Gao, J.; Shang, H. Deformation-pattern-based digital image correlation method and its application to residual stress measurement. *Appl. Opt.* **2009**, *48*, 1371–1381. [CrossRef] [PubMed]
21. McGinnis, M.J.; Pessiki, S.; Turker, H. Application of three-dimensional digital image correlation to the core-drilling method. *Exp. Mech.* **2005**, *45*, 359–367. [CrossRef]
22. McGinnis, M.J.; Pessiki, S. Experimental study of the core-drilling method for evaluating in situ stresses in concrete structures. *J. Mater. Civ. Eng.* **2016**, *28*, 04015099. [CrossRef]
23. Deng, S.Q. Study on Stress Measurement Method of Hydraulic Concrete Based on Digital Image Correlation Method and Stress Release Method. Master's Thesis, Chongqing Jiaotong University, Chongqing, China, 2017.
24. Peng, Y.; Zhao, J.; Chen, L.; Deng, J. DIC-hole drilling method for in-situ residual stress measurement. In Proceedings of the 1st International Conference on Advances in Civil Engineering and Materials (ACEM1) and 1st World Symposium on Sustainable Bio-composite Materials and Structures (SBMS1) (ACEM2018 and SBMS1), Nanjing, China, 9–11 November 2018; Volume 275, p. 02004.
25. Lee, J.; Kim, E.J.; Gwon, S.; Cho, S.; Sim, S.-H. Uniaxial static stress estimation for concrete structures using digital image correlation. *Sensors* **2019**, *19*, 319. [CrossRef] [PubMed]
26. Allain, M.; Ple, O.; Prime, N.; Roux, E.; Vacher, P. In situ DIC method to determine stress state in reinforced concrete structures. *Measurement* **2023**, *210*, 112483. [CrossRef]
27. Qin, Y.; Zhao, S.; Zhou, H.; Zhao, J.; Wu, J. Splitting Damage Process and Law of Steel Fiber Reinforced Concrete Based on Digital Image and Ultrasonic Technology. *J. Chin. Ceram. Soc.* **2025**, *53*, 2287–2300.
28. Xu, Z.L. *Elasticity*; Higher Education Press: Beijing, China, 2016.

29. Wang, L.J.; Pan, L.Z.; Liao, C.T.; Ding, Y.; Qu, M. *In-Situ Stress Measurement and Its Application in Engineering*; Geological Publishing House: Beijing, China, 1991.
30. Liang, X. Research on Monitoring and Early Warning Technology for Water-Rich Tunnel Lining Structures Based on Machine Learning. Master's Thesis, Chongqing Jiaotong University, Chongqing, China, 2024.

Disclaimer/Publisher's Note: The statements, opinions and data contained in all publications are solely those of the individual author(s) and contributor(s) and not of MDPI and/or the editor(s). MDPI and/or the editor(s) disclaim responsibility for any injury to people or property resulting from any ideas, methods, instructions or products referred to in the content.